# Experimental Investigation of Drop Detachment and Drop Velocity in GMAW

*The drop velocity at detachment is controlled by Lorentz force acting after the liquid tip has become unstable*

**BY J. H. WASZINK AND M. J. PIENA**

ABSTRACT. The velocity of drops detached from a consumable wire during GMA welding and the diameter of the drop neck during the detachment process were measured with the aid of high-speed photography. Wire materials were mild steel, AlMg5 and AlSi5. Most of the measurements were made with a pulsed current; drop transfer was of the globular type. It was found that the pendent drop contracts when the pulse starts and that it becomes unstable when its diameter reaches a certain critical value. The velocity at detachment from mild steel wire can be ascribed to electromagnetic forces acting after the drop has become unstable. Another additional mechanism must be operative when the wire material is one of the aluminum alloys. This mechanism was not identified with certainty. The acceleration of the drops in the arc after detachment can be ascribed to a gradient in the plasma pressure, also caused by electromagnetic effects. Analysis of the heat balance indicates that the drop temperature is lower in pulsed welding than it is in welding at a constant current.

## Introduction

The processes of fluid flow and heat transfer in the weld pool are of great practical interest because they affect the properties of the weld bead which eventually results. In welding processes with nonconsumable electrodes, the physical phenomena that lead to fluid flow in the weld pool are primarily the electromagnetic and the surface tension forces (Ref. 1). Investigations of the gas metal arc (GMA) process (Refs. 2a, 2b) showed that the depth of the weld pool is strongly influenced by the impact of the drops of metal that are detached from the consumable wire. This means that a quantitative description of the heat and mass flow in the weld pool during GMA welding will have to include as a major effect the force exerted by the incoming drops on the liquid metal in the weld pool. Thus, the question arises: Which variables control the mass and the velocity of the drops? The work presented here deals with the drop velocity.

Previous measurements of the drop velocity in GMA (Refs. 3-7) and plasma-GMA (Ref. 1) arcs lead to the following conclusions. Firstly, the drops already have an appreciable velocity at the moment of detachment from the wire tip, and this velocity depends on the electric current, I, and on the drop mass, M. Secondly, the drops are accelerated in the arc, and the acceleration also depends on I and M. Thirdly, there is no discontinuity in the acceleration at the moment of detachment (Ref. 7).

A theoretical treatment of the physical mechanism which controls the velocity at detachment was given by Lancaster (Ref. 8), who extended a model developed by Murty (Ref. 9). This treatment provides orders of magnitude, but experimentally it has been verified only to a limited extent.

Consequently, it can be said that the physical processes that control the drop velocity are important because of their effect on weld pool penetration, but that they are not well understood yet. The aim of the work described below was to provide insight into the processes that govern the velocity at detachment. This velocity was measured and a simple model of the process of acceleration was developed. Some measurements were also made of the velocity after detachment, and the data collected on the melting rate provide information on the drop temperature.

Most of the previous experiments (Refs. 3-6) were carried out with DC wire current. This means that M and I can only be varied independently if the extension length is also varied. A pulsed current was applied in the experiments described below, in order to extend the possibility to vary M and I independently, and also in order to avoid spray-type transfer at high currents. A pulsed current was also used by Jilong Ma and Apps (Ref. 7).

The physical model for the acceleration of the pendent drop is based on the result, obtained by Maecker (Ref. 10), that a fluid flow is generated in, and a volume force is exerted on, a liquid or gaseous conductor if a diverging current passes through that conductor (see also Refs. 11, 12).

## Experiments

Mild steel electrode wire (0.10% C, 1.5% Mn, 0.9% Si; AWS A5.18, ER 70S-6; wire diameter $d_w$, 1.2 mm = 0.047 in. and 1.6 mm = 0.063 in.), AlMg5 wire (4.5-5.5% Mg; ASTM B285, ER 5356; $d_w$ = 1.6 mm), and AlSi5 wire (4.5-5.5% Si; ASTM B285, 4043; $d_w$ = 1.6 mm) were used with pure argon shielding gas (18 l/min − 8.5 cfh) in a conventional GMA torch. Wire polarity was positive. The distance between contact tube and wire tip was always between 10 and 30 mm (0.4 and 1.2 in.), and the arc length was between 5 and 15 mm (0.2 and 0.6 in.). A transistor power source (ripple <0.5%) was used in the current-controlled mode, and square-wave current pulses were superimposed on a continuous background current. The current waveform and the wire speed, $v_w$, were chosen such that one drop was detached per current pulse, and the drop was detached before the end of the pulse. The drop mass was derived from $v_w$ and the pulse frequency (10 − 100 Hz).

The drop velocity was obtained from a curve of axial position as a function of time. This curve was obtained from photographs made with the arrangement shown in Fig. 1. A He-Ne laser (wavelength 633 nm, 5 mW) was used as the background light source.

*J. H. WASZINK and M. J. PIENA are with Philips Research Laboratories, Eindhoven, Netherlands.*

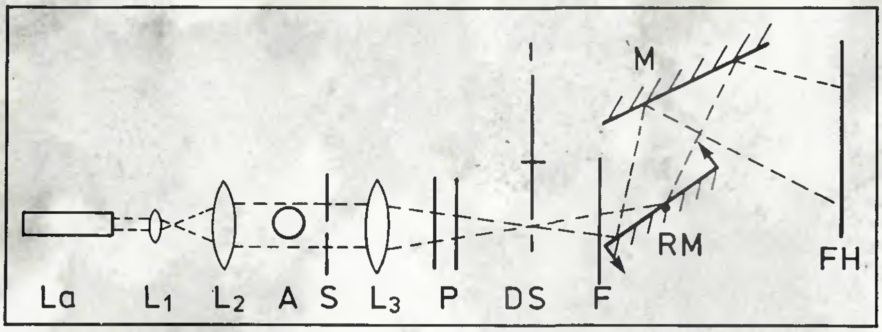


Fig. 1 — Schematic diagram of photographic arrangement. La — laser; $L_1$, $L_2$, $L_3$ — lenses ($L_1$ and $L_2$ form a beam expander); A — welding arc; S — slit; P — polarizer; DS — disc shutter; F — optical filter; RM — rotating mirror; M — fixed mirror; FH — film holder

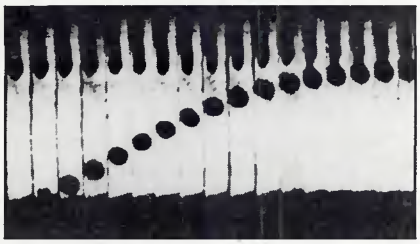

Fig. 2 — Part of photograph obtained with arrangement of Fig. 1. Time between successive frames is 1.6 ms. Mild steel wire, $d_w$ = 1.2 mm = 0.047 in., I = 207 A DC, M = 42 mg, $v_w$ = 88 mm/s = 208 ipm

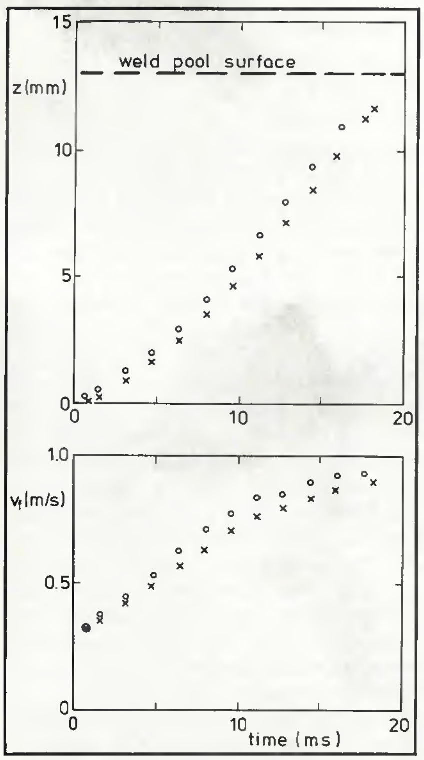


Fig. 3 — Axial position and velocity of drop after detachment. Arbitrary zero for z. Plots are given for two drops measured successively at the same setting as for Fig. 2. o — $a_i$ = 41 m/s²; x — $a_i$ = 33 m/s²

The image of the arc, limited by a 2-mm slit, was projected on the film by a rotating mirror, so that the image was swept along the film. A rotating disc (diameter 100 mm/3.9 in.) provided with 16 holes (diameter 2 mm/0.08 in.) near the edge acted as the shutter. It was placed in the focal plane of the lens (L) — Fig. 1. A similar arrangement was used by Needham (Ref. 13). A narrow-band optical filter (spectral half width 1 nm), transmitting light at the laser wavelength, rejected nearly all the light from the arc. Two polarizers were used to adjust the light intensity. The advantage of this arrangement above conventional high-speed cinematography is that an instant film (3000 ASA, 3¼ × 4 in.) can be used, while the number of frames per picture is sufficient (up to 50).

The vertical position, z, was measured on the images — Fig. 2. It was taken as the average between top and bottom of the drop. The velocity at detachment was determined graphically from plots of z *vs.* time, t — Fig. 3. Tables 1–5 give the drop velocity with respect to the moving wire at the moment of detachment, $v_i$, *i.e.*, the velocity determined from the plots minus $v_w$. These data show that $v_i$ depends on M and on the total current during the pulse, $I_p$ (pulse + background), and that $v_i$ is higher for the aluminum alloys than for the mild steel.

Some measurements were made of the velocity of the falling drop after detachment, $v_f$, during DC operation with mild steel wire. A least squares parabola was then laid through five successive points on the z *vs.* t curve, and the tangent was taken at the center point (Ref. 14).

It was found that $v_f$ increased practically linearly with t immediately after detachment — Fig. 3. The acceleration at the moment of detachment was determined graphically from the curve of $v_f$ *vs.* t. The acceleration $a_i$ (Table 6) is the measured initial acceleration minus the gravity constant, *i.e.*, the acceleration of the drop by the plasma.

**Table 1—Drop Velocity with Respect to Moving Wire at Detachment**

| $I_{av}$(a) (A) | $I_p$ (A) | M (mg) | $v_w$(a) (m/s) | $v_i$ (m/s) |
|---|---|---|---|---|
| 70 | 200 | 23.6 | 0.039 | 0.39 |
| 70 | 200 | 15.7 | 0.039 | 0.46 |
| 70 | 200 | 8.3 | 0.041 | 0.56 |
| 70 | 200 | 6.6 | 0.044 | 0.73 |
| 70 | 250 | 23.6 | 0.039 | 0.71 |
| 70 | 250 | 16.0 | 0.040 | 0.83 |
| 70 | 250 | 8.6 | 0.043 | 0.93 |
| 70 | 250 | 7.1 | 0.047 | 1.05 |
| 70 | 330 | 18.0 | 0.045 | 1.09 |
| 70 | 330 | 10.2 | 0.051 | 1.33 |
| 70 | 330 | 9.9 | 0.049 | 1.18 |
| 130 | 250 | 16.4 | 0.082 | 0.58 |
| 130 | 250 | 8.6 | 0.086 | 0.83 |
| 130 | 330 | 17.1 | 0.085 | 1.05 |
| 130 | 330 | 8.8 | 0.088 | 1.34 |
| 130 | 330 | 6.4 | 0.095 | 1.55 |
| 130 | 370 | 16.6 | 0.083 | 1.18 |
| 130 | 370 | 9.4 | 0.094 | 1.45 |

(a) $I_{av}$ is the time average of the current and $v_w$ is the wire velocity. Mild steel $d_w$ = 1.0 mm.

In order to study the detachment process, conventional high-speed films (9000 frames per second) were made during pulsed operation, with the laser as the background light source, and the optical filter in front of the camera. The wire tip is clearly visible on these images, while the arc is just visible — Figs. 4 and 5. Following the chemical literature on drop detachment from capillary tubes, we will use the term "pendent drop" (hanging drop) for the liquid metal at the wire tip before drop detachment.

These films show that the pendent drop becomes elongated after the start of the pulse, that a neck is formed after some time (Figs. 4 and 5), and that the radius of this neck, $R_n$, then rapidly decreases to zero. Furthermore, the results show that $R_n^2$ decreases linearly with time once $R_n$ has reached some critical value — Figs. 4–6. The results can be represented by

$$\left(\frac{R_n}{R_w}\right)^2 = \left(\frac{R_c}{R_w}\right)^2 - \alpha\,(t - t_c) \qquad (1)$$

for $t > t_c$, where $R_w$ is the wire radius and $R_c$ the critical neck radius at the moment ($t = t_c$) that $R_n^2$ becomes linear with t, and $\alpha$ is a constant; the start of the current pulse is taken as t = 0. Table 7 gives $R_c$ and $\alpha$ as determined from plots as given in Figs. 4–6.

There was a considerable spatter during the experiments with AlMg5 wire, drops often exploding before detachment, as was also observed by Woods (Ref. 15). Nevertheless, the curves of $R_n^2$ *vs.* t for this alloy were very smooth — Fig. 6.

Table 8 gives the experimental data used in the analysis of the heat balance of the process during welding with mild

Table 2—As Table 1 for Mild Steel, $d_w$ = 1.2 mm

| $I_{av}$ (A) | $I_p$ (A) | M (mg) | $v_w$ (m/s) | $v_i$ (m/s) |
|---|---|---|---|---|
| 70 | 180 | 24.2 | 0.028 | 0.32 |
| 70 | 180 | 32.2 | 0.028 | 0.38 |
| 70 | 250 | 24.2 | 0.028 | 0.53 |
| 70 | 250 | 11.5 | 0.028 | 0.68 |
| 70 | 250 | 8.1 | 0.028 | 0.87 |
| 70 | 270 | 11.1 | 0.026 | 0.80 |
| 70 | 330 | 29.7 | 0.026 | 0.81 |
| 70 | 330 | 19.4 | 0.028 | 0.72 |
| 70 | 330 | 14.9 | 0.026 | 1.20 |
| 70 | 330 | 11.9 | 0.027 | 1.41 |
| 70 | 330 | 8.7 | 0.030 | 1.53 |
| 130 | 250 | 48.4 | 0.056 | 0.44 |
| 130 | 250 | 24.2 | 0.056 | 0.48 |
| 130 | 250 | 12.1 | 0.056 | 0.69 |
| 130 | 330 | 34.3 | 0.056 | 0.60 |
| 130 | 330 | 22.0 | 0.051 | 0.69 |
| 130 | 330 | 15.5 | 0.053 | 0.88 |
| 130 | 330 | 11.7 | 0.054 | 1.01 |
| 130 | 330 | 8.4 | 0.058 | 1.36 |
| 130 | 330 | 6.7 | 0.062 | 1.39 |
| 130 | 370 | 12.1 | 0.056 | 1.19 |
| 180 | 250 | 49.5 | 0.080 | 0.37 |
| 180 | 250 | 21.6 | 0.075 | 0.57 |
| 180 | 250 | 10.6 | 0.073 | 0.76 |
| 180 | 330 | 46.1 | 0.073 | 0.64 |
| 180 | 330 | 22.6 | 0.078 | 0.77 |
| 180 | 330 | 11.6 | 0.080 | 1.09 |
| 180 | 330 | 8.2 | 0.085 | 1.20 |
| 180 | 330 | 6.3 | 0.087 | 1.61 |
| 180 | 370 | 11.6 | 0.080 | 1.25 |

Table 3—As Table 1 for Mild Steel, $d_w$ = 1.6 mm

| $I_{av}$ (A) | $I_p$ (A) | M (mg) | $v_w$ (m/s) | $v_i$ (m/s) |
|---|---|---|---|---|
| 130 | 250 | 22.3 | 0.029 | 0.50 |
| 130 | 250 | 14.9 | 0.029 | 0.60 |
| 130 | 330 | 24.0 | 0.034 | 0.93 |
| 130 | 330 | 12.0 | 0.034 | 1.18 |
| 180 | 250 | 32.7 | 0.042 | 0.47 |
| 180 | 330 | 32.6 | 0.042 | 0.63 |
| 180 | 330 | 16.3 | 0.042 | 0.91 |
| 180 | 330 | 11.4 | 0.044 | 0.97 |
| 180 | 370 | 12.4 | 0.048 | 1.21 |
| 230 | 330 | 46.3 | 0.059 | 0.67 |
| 230 | 330 | 30.9 | 0.059 | 0.71 |
| 230 | 330 | 15.7 | 0.060 | 0.95 |
| 230 | 330 | 10.7 | 0.061 | 1.12 |
| 230 | 370 | 30.9 | 0.059 | 0.78 |
| 230 | 370 | 15.4 | 0.059 | 1.17 |
| 230 | 410 | 46.3 | 0.059 | 0.92 |
| 230 | 410 | 15.9 | 0.061 | 1.35 |

Table 4—As Table 1 for AlMg5, $d_w$ = 1.6 mm

| $I_{av}$ (A) | $I_p$ (A) | M (mg) | $v_w$ (m/s) | $v_i$ (m/s) |
|---|---|---|---|---|
| 100 | 250 | 13.7 | 0.052 | 1.68 |
| 150 | 250 | 9.9 | 0.075 | 1.65 |
| 150 | 250 | 6.5 | 0.074 | 1.93 |
| 150 | 290 | 6.6 | 0.076 | 2.19 |
| 150 | 330 | 10.2 | 0.077 | 2.15 |
| 150 | 330 | 6.8 | 0.077 | 2.52 |
| 150 | 330 | 4.8 | 0.083 | 2.50 |

Table 5—As Table 1 for AlSi5, $d_w$ = 1.6 mm

| $I_{av}$ (A) | $I_p$ (A) | M (mg) | $v_w$ (m/s) | $v_i$ (m/s) |
|---|---|---|---|---|
| 50 | 200 | 4.1 | 0.023 | 1.96 |
| 50 | 250 | 4.3 | 0.024 | 2.62 |
| 100 | 200 | 12.1 | 0.047 | 1.32 |
| 100 | 200 | 5.8 | 0.044 | 1.70 |
| 100 | 290 | 13.1 | 0.050 | 1.69 |
| 100 | 290 | 6.0 | 0.045 | 2.48 |
| 150 | 250 | 8.2 | 0.062 | 1.84 |
| 150 | 290 | 8.5 | 0.065 | 2.03 |
| 150 | 330 | 8.6 | 0.064 | 2.44 |

Table 6—Acceleration of Drop by Plasma Immediately after Detachment

| I (A) | M (mg) | $a_i$[(a)] (m/s$^2$) |
|---|---|---|
| 198 | 44 | 33 |
| 198 | 61 | 27 |
| 207 | 42 | 37 |
| 207 | 22 | 38 |
| 207 | 22 | 33 |
| 217 | 17 | 60 |

(a) Mild steel, $d_w$ = 1.2 mm, DC operation; $a_i$ is average over several drops.

steel wire, *viz.* the melting rate $\mu$ (*i.e.*, the mass of metal melted per unit time), the time average of the current, $I_{av}$, the effective current $I_{eff}$ (*i.e.*, the square root of the average of the square of the current), and the length of the current-carrying part of the solid wire, $L_s$. The length $L_s$, *i.e.*, the distance between the contact tube and the pendent drop, was determined from the photographs and the torch geometry.

### Process of Drop Detachment

The experiments show that, after the start of the current pulse, the pendent drop is elongated and contracts until a neck is formed. The radius of this neck then decreases rapidly to zero—Figs. 4-6.

The following strongly simplified model will be used to describe the detachment process. The drop is cylindrical at t = 0, and the current does not diverge in it, so that there is no axial Lorentz force. There is a radial Lorentz force, which causes the cylinder to contract, so that the ratio of the length of the cylinder, $L_d$, to its radius, $R_d$, increases. We assume that the cylinder becomes unstable when this ratio exceeds a certain critical value. This hypothesis was also made by Lancaster (Ref. 8). It is based on the following argument.

A conducting infinite liquid cylinder, having a radius $R_d$, which carries an electric current $I_p$, is unstable with respect to a sinusoidal perturbation of its surface (Ref. 16). This type of instability is known as a sausage instability. The wavelength of the perturbation, $\lambda$, is given by (Ref. 17)

$$\lambda = \frac{2\,\pi\,R_d}{1 + \left(\dfrac{\mu_0\, I_p^2}{2\pi^2\, R_d\, \gamma}\right)^{1/2}} \qquad (2)$$

where $\mu_0$ is the permeability of vacuum, and $\gamma$ the surface tension. Data on the magnetic susceptibility of liquid iron (Ref. 18) show that the magnetic permeability is approximately equal to $\mu_0$ $(1 + 2 \times 10^{-4}) \approx \mu_0$, so that $\mu_0$ is used in Equation 2.

It is now assumed that the pendent cylindrical drop becomes unstable when the ratio $L_d/\lambda$ begins to exceed some fixed value, which is close to unity. When electromagnetic effects are dominant, then the first term in the denominator in Equation 2 is negligible compared with the second, and the condition for instability becomes

$$\frac{L_d}{R_d} > \text{const.}\ \frac{R_d^{1/2}}{I_p} \qquad (3)$$

Since $M = \pi\, R_d^2\, L_d\, \rho$, where $\rho$ is the mass density, we may write Equation 3 as

$$R_d < R_{cr} \equiv \beta\, (M\, I_p)^{2/7} \qquad (4)$$

where $\beta$ is a material constant and $R_{cr}$ a critical radius defined by Equation 4. Using Equation 2 to obtain an order of magnitude, we find that $\beta$ is expected to lie between $10^{-3}$ and $10^{-2}$ SI units, and to be proportional to $\rho^{-2/7}\,\gamma^{-1/7}$, where $\rho$ is the mass density. With the data in Table 9 we thus obtain $\beta_{Al}/\beta_{ms} \approx 1.4$, where $\beta_{Al}$ and $\beta_{ms}$ are the values of $\beta$ for pure aluminum and mild steel, respectively.

We now identify $R_{cr}$ (Equation 4) with $R_c$ as defined in the previous section, and derive $\beta$ from the measured data—Table 7. These results show that the order of magnitude of $\beta$ is as expected, that $\beta_{AlMg}/\beta_{ms}$ = 1.6, and that $\beta_{AlSi}\beta_{ms}$ = 1.5, in reasonable agreement with the model.

The available data do not allow the verification of Equation 4 by a plot of experimental data on $R_c$ *vs.* $(MI)^{2/7}$, because the measured values of these quantities lie within very narrow ranges. On the other hand, it can be said that the available data agree with the model given above.

Next, we will discuss the detachment process, which starts when a neck is formed ($R_n = R_c$). The first question is which variables affect the quantity $\alpha$, since this is a measure of the growth rate

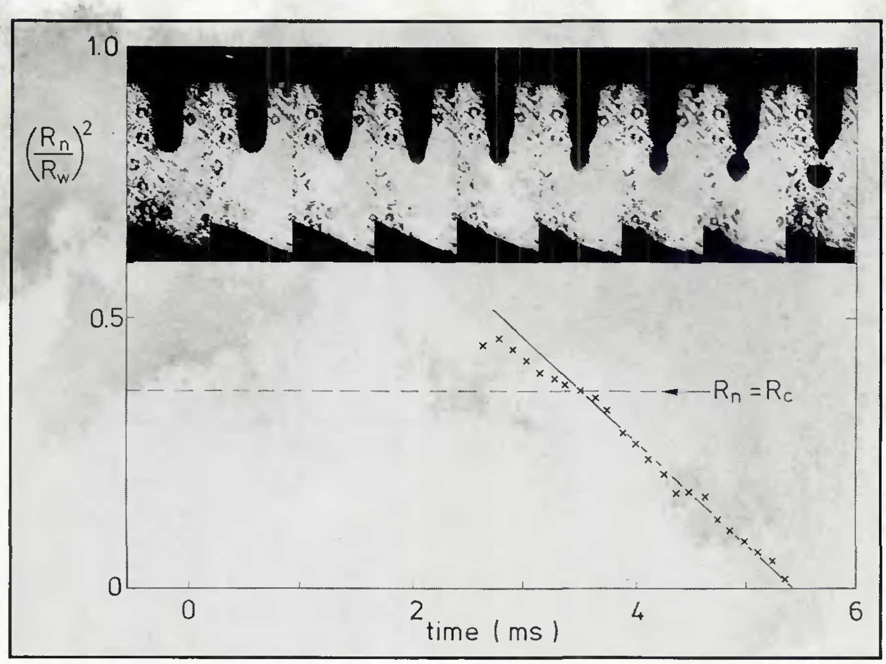


*Fig. 4—Drop shape and relative cross-sectional area of drop neck. Current pulse starts at t = 0. Mild steel, $d_w$ = 1.6 mm = 0.063 in., $I_p$ = 330 A, M = 9.7 mg. The time point for a frame is the horizontal coordinate of its center*

of the instability. Equation 1 gives

$$\alpha = -\frac{2R_n}{R_w^2} \cdot \frac{dR_n}{dt} \qquad (5)$$

Analysis of the equations that describe fluid flow in electrically conducting fluids (Ref. 19) shows that the flow velocity, u, scales as

$$u \propto \frac{I_p}{L}\sqrt{\frac{\mu_0}{\rho}} \qquad (6)$$

where L is a typical length, taken here as $L = R_c$. Relation 6 holds if the effect of the fluid flow on the electric current is negligible, *i.e.*, if the variable $K = \mu_0^{3/2}\,\sigma\, I_p/\rho^{1/2}$, as introduced by Shercliff (Ref. 19), is small compared with unity ($\sigma$ is the electric conductivity). Using the data in Table 9, we find $K \approx 10^{-3}$ for iron, and $K \approx 10^{-2}$ for Al. The latter value is an upper limit for the Al alloys, because their conductivity will be less than that of Al. Consequently, it is justified to assume that $K \ll 1$.

Since $dR_n/dt$ is of order u, we expect, on the basis of Equations 5 and 6, that the growth rate $\alpha$ will, for geometrically similar systems, vary as

$$\alpha = \psi \frac{I_p}{\pi R_w^2}\sqrt{\frac{\mu_0}{\rho}} \qquad (7)$$

where $\psi$ is a dimensionless constant. It is, however, doubtful whether the pendent drop on an aluminum wire is geometrically similar to that on a mild steel wire, because a sharp conical tip is formed on the solid steel wire (Refs. 20, 21), while such a sharp tip has, to the authors' knowledge, not been observed on aluminum wire.

Figure 7 shows the measured values of $\alpha$ (Table 1) as a function of $j_p\sqrt{\mu_0/\rho}$, where $j_p = I_p/(\pi R_w^2)$. This figure shows that the dependence of $\alpha$ on $j_p$ is as given by Equation 7, but that the dependence of $\alpha$ on $\rho$ is not, as the curves for the different materials do not coincide.

It is also of interest to consider results obtained by Lev and Peregud (Ref. 22). They passed very high currents (up to 23 kA) through 0.5-mm (0.02-in.) diameter copper wires and measured the time ($t_{ex}$) needed for break-up of the wire from the moment it melted, *i.e.*, from the moment the sausage instability began to develop. A plot of the quantity $t_{ex}^{-1}$, which is comparable with $\alpha$, is also linear with $j_p$ up to $j_p = 9 \times 10^{10}$ A/m$^2$. Reference 22 does not give this plot, but it is readily prepared from Table 1. Figure 7 also shows the extrapolation of their curve down to low current densities. It is seen to lie close to the curves for the Al alloys.

The curves in Fig. 7 give $\psi = 0.10$ for mild steel, $\psi = 0.15$ for AlMg5, and $\psi = 0.22$ for AlSi5. The difference between these values might be due to differences in tip geometry, as discussed above, but other possible causes have to be considered as well.

The differences in $\psi$ cannot be ascribed to the difference in $\sigma$, because this property plays no role at low K. Neither can they be ascribed to a difference in viscosity, as the Reynolds number, $Re = u \cdot L/\upsilon$, is about 2000 ($\upsilon$ is the kinematic viscosity, and $u \approx 1$ m/s $\approx$ 2400 ipm, $L \approx 1$ mm $\approx$ 0.04 in.), so that viscous forces are negligible.

Another possibility is that a part of the current $I_p$ bypasses the neck. However, the high-speed films show that the arc anode jumps from the lower drop surface onto the liquid above the neck only on the very last frames (0.1 to 0.2 ms)

**Table 7—Parameters Describing Detachment Process, Determined by Measurements on High-Speed Films**

| Material | $d_w$ (mm) | $I_p$ (A) | M (mg) | $R_c$[a] (mm) | $\alpha$[a] $10^3 s^{-1}$ | $R_c/(M\,I_p)^{2/7}$ $10^{-3}$ m.k.s. units |
|---|---|---|---|---|---|---|
| Mild steel | 1.0 | 250 | 18.2 | 0.38 | 0.51 | 1.9 |
| | 1.0 | 250 | 8.3 | 0.46 | 0.41 | 2.7 |
| | 1.0 | 370 | 9.4 | 0.47 | 0.69 | 2.4 |
| | 1.6 | 330 | 9.7 | 0.47 | 0.20 | 2.4 |
| | 1.6 | 370 | 10.9 | 0.48 | 0.27 | 2.3 |
| AlMg5 | 1.6 | 250 | 10.2 | 0.70 | 0.42 | 3.8 |
| | 1.6 | 330 | 10.8 | 0.72 | 0.63 | 3.6 |
| AlSi5 | 1.6 | 250 | 8.4 | 0.59 | 0.65 | 3.4 |
| | 1.6 | 330 | 9.0 | 0.65 | 0.88 | 3.4 |

(a)Values of $R_c$ and $\alpha$ are averages over 2–4 drops.

**Table 8—Experimental Data on Pulsed GMA Welding. Mild steel, $d_w$ = 1.2 mm**

| $\mu$ (g/s) | $I_{av}$ (A) | $I_{eff}$ (A) | $L_s$ (mm) |
|---|---|---|---|
| 0.70 | 180 | 183 | 11 |
| 0.48 | 130 | 147 | 16 |
| 0.48 | 130 | 143 | 17 |
| 0.48 | 130 | 138 | 9 |
| 0.49 | 130 | 158 | 15 |
| 0.61 | 130 | 156 | 27 |
| 0.44 | 130 | 150 | 11 |
| 0.61 | 170 | 187 | 13 |
| 0.43 | 100 | 131 | 27 |
| 0.48 | 130 | 135 | 21 |
| 0.70 | 180 | 183 | 17 |
| 0.70 | 180 | 186 | 16 |
| 0.48 | 130 | 178 | 10 |
| 0.46 | 130 | 152 | 14 |
| 0.50 | 130 | 180 | 12 |
| 0.44 | 130 | 143 | 12 |
| 0.75 | 180 | 231 | 13 |
| 0.70 | 180 | 197 | 15 |
| 0.74 | 180 | 219 | 14 |
| 0.68 | 180 | 190 | 14 |
| 0.64 | 180 | 189 | 12 |

before rupture. Nevertheless, we will consider the possibility that the current through the neck, $I_n$, is less than the wire current $I_p$, because film images do not give conclusive evidence on the current path. Consequently, there are two possibilities. The first is that all the current passes through the neck and $\psi$ are different for the three wire materials, having the values given above. The second possibility is that $I_n < I_p$ for the mild steel and for AlMg5, and that $\psi$ is the same for all the materials if $I_p$ is replaced by $I_n$ in Equation 7. Assuming that $I_n = I_p$ for AlSi5 (*i.e.*, the material with the highest $\psi$-value), we obtain $q = I_n/I_p = 0.7$ for AlMg5 and $q = 0.45$ for mild steel. These two possibilities will be considered in the analysis of the velocity at detachment.

### Drop Velocity at Detachment

This section deals with the acceleration of the pendent drop during the high-current period and the resulting velocity at detachment.

The dominant detaching force is the Lorentz force, $\vec{f}_L$, due to the interaction of the current with its own magnetic field (Refs. 10–12). It is given by

$$\vec{f}_L = \vec{j} \times \vec{B} \qquad (8)$$

where $\vec{f}_L$ is the force per unit volume, $\vec{j}$ is the current density and $\vec{B}$ is the magnetic induction. In a cylindrical liquid conductor, the radial component $f_{Lr}$ (coordinates as in Fig. 8) is non-zero, which causes an excess pressure, $p_L$, above the ambient pressure, $p_0$. If j is constant, then (Ref. 17)

$$p_L(r) = \frac{\mu_0 I_n^2}{4\pi^2 R^2}\left(1 - \frac{r^2}{R^2}\right) \qquad (9)$$

where r is the radial coordinate and R is the cylinder radius. As a rule, the current diverges within the drop and within the arc. The pressure $p_L$ then also varies with the axial (z) coordinate—Fig. 8. It decreases towards widening current path, and thus causes a fluid flow in that direction. Measurements of the flow velocity in arcs give values of 100 to 1000 m/s (Refs. 23, 24). The kinetic pressure corresponding to these velocities is so high that the static pressure in the arc must be close to $p_0$ (Ref. 25). The flow velocity within the drop (Ref. 26) is low and the static pressure will be practically equal to $p_0 + p_L$ (r), if the effects of surface tension are neglected. The pressure difference between drop and arc thus causes a downward force on the drop, *i.e.*, directed towards the arc, given by

$$F_1 = \int_0^R 2\pi r \, p_L(r) \, dr = \frac{\mu_0 I^2}{8\pi} \qquad (10)$$

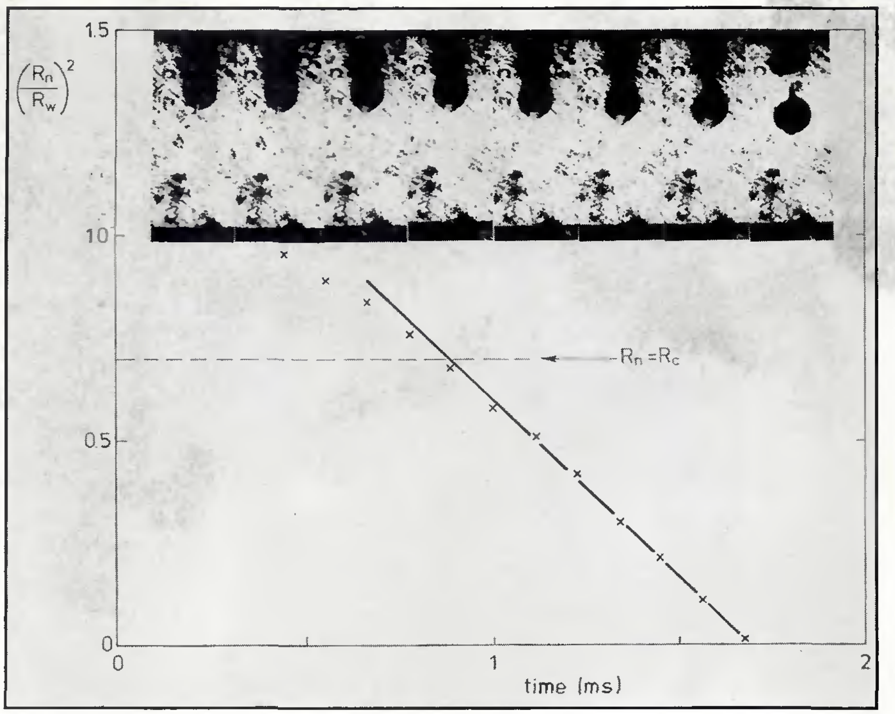


*Fig. 5—As Fig. 4 for AlSi5; $d_w$ = 1.6 mm, $I_p$ = 330 A, M = 9.0 mg*

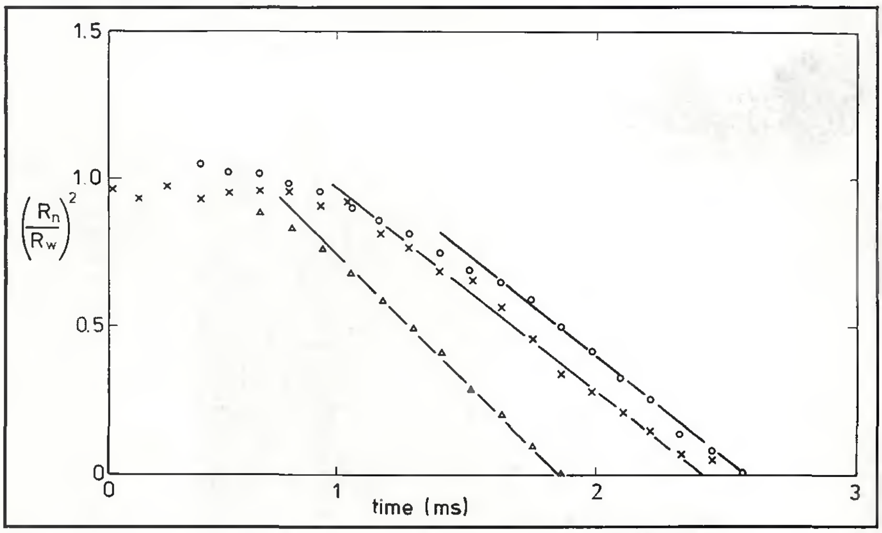


*Fig. 6—Relative cross-sectional area of drop neck as a function of time. x—mild steel, $d_w$ = 1.0 mm, $I_p$ = 370 A, M = 9.4 mg; o—AlMg5, $d_w$ = 1.6 mm, $I_p$ = 330 A, M = 10.8 mg; Δ—AlSi5, $d_w$ = 1.6 mm, $I_p$ = 330 A, M = 9.0 mg*

Consequently, $F_1$ is the downward force on the pendent drop if the electric current does not diverge in the drop and does diverge in the arc.

When the current diverges within the drop, the axial component $f_{Lz}$ is non-zero as well. The current-carrying volume is then, approximately, a truncated cone, and integration of $f_{Lz}$ over this volume gives a downward force on the drop (Ref. 10)

$$F_2 = \frac{\mu_0 I^2}{4\pi} \ln \frac{R_l}{R_u} \qquad (11)$$

**Table 9—Approximate Values of Physical Properties of Liquid Fe and Al, Used for Wire Materials**

| Property and Unit | Fe | Al |
|---|---|---|
| $\rho$ (kg m$^{-3}$) | 6500 | 2200 |
| $\sigma$ ($10^6$ $\Omega^{-1}$ m$^{-1}$) | 0.71 | 4.0 |
| $\upsilon$ ($10^{-6}$ m$^2$ s$^{-1}$) | 0.6 | 0.5 |
| $\gamma$ (J m$^{-2}$) | 1.0 (mild steel) | 0.8 |

Data from Ref. 30, except $\gamma$ for mild steel (Ref. 25).

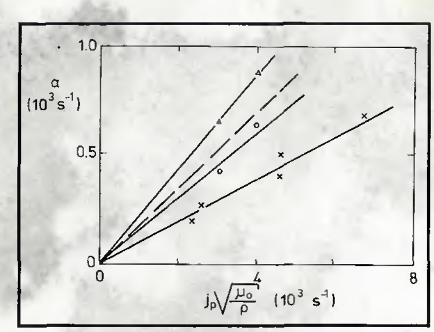


*Fig. 7—Plot of experimental data to verify model of drop detachment. Data from Table 7. x—mild steel; o—AlMg5; Δ—AlSi5; broken line—extrapolation of curve of $t_{ex}^{-1}$ for Cu (Ref. 22)*

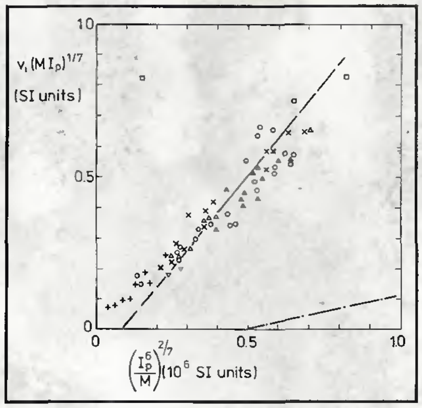


*Fig. 9—Plot of experimental data, drawn to verify model of acceleration of pendent drop, Equation 19. Mild steel, $R_c < R_w$; $\psi = 0.10$. $x - d_w = 1.0$ mm; $o - d_w = 1.2$ mm; $\Delta - d_w = 1.6$ mm. ∇ and + — data from Refs. 4 and 6, respectively (wire positive). □— data from Ref. 3 (wire negative). — — — Equation 19 with q = 1. — · — Equation 19 with q = 0.45*

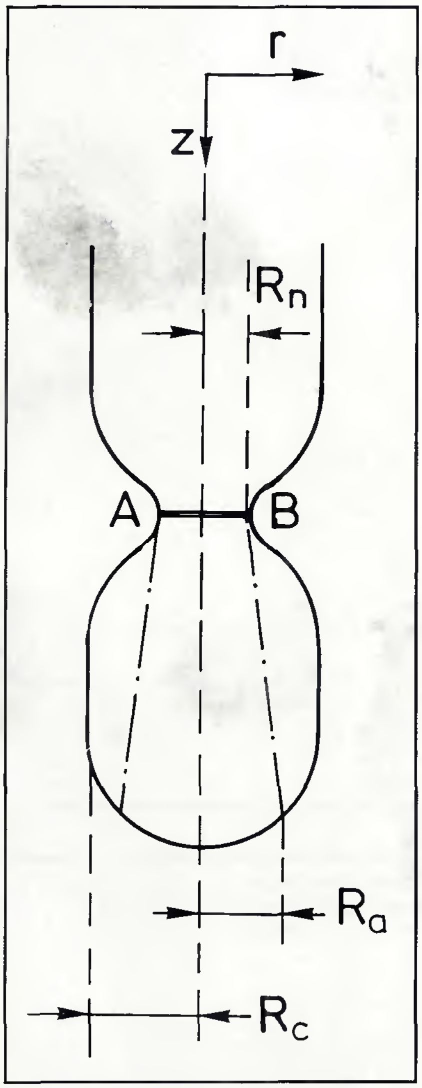


*Fig. 8—Illustration of discussion of forces on pendent drop. — · — boundary of current-carrying volume*

where $R_l$ and $R_u$ are the radii of the lower and upper base of the cone, respectively. For a more detailed treatment of spherical drops, see Refs. 11 and 12.

The total electromagnetic force on the drop then becomes

$$F_{em} = F_1 + F_2 = \frac{\mu_0\, I^2}{4\P}\left(\tfrac{1}{2} + \ln\frac{R_l}{R_u}\right) \quad (12)$$

When $t < t_c$, the drop is either cylindrical or conical and narrowing towards the arc—Figs. 4 and 5. We then have $R_u = R_w$, while $R_l$ is equal to the radius of the anode area, $R_a$, and $I = I_p$, so that

$$F_{em} = \frac{\mu_0\, I_p^2}{4\P}\left(\tfrac{1}{2} + \ln\frac{R_a}{R_w}\right) \quad (13)$$

Since $R_a < R_w$, the terms within the brackets have opposite signs, so that $F_{em}$ is extremely sensitive to small variations in $R_a$. As detailed information on $R_a$ is lacking, it is impossible to make any prediction of $F_{em}$ at this stage. The experimental result that the drop is elongated indicates that $F_{em}$ is positive.

When $t > t_c$, a neck is formed—Fig. 8. For the part of the drop that is going to be detached (below AB in Fig. 8) we now have $R_u = R_n$, $R_l = R_a$, and $I = I_n$. Taking $R_a$ to be equal to the radius of the elongated drop and the latter equal to $R_c$, we obtain

$$F_{em} = \frac{\mu_0\, I_n^2}{4\P}\left(\tfrac{1}{2} + \ln\frac{R_c}{R_n}\right) \quad (14)$$

The surface tension force, $F_\gamma$, which opposes detachment, is taken to be (Ref. 25)

$$F_\gamma = 2\,\pi\,R_n\,\gamma \quad (15)$$

Other forces acting on the drop are the gravity force, M g (g is the gravity constant), the force exerted by the metal entering the drop, $\mu\ v_w$, and the drag force exerted by the gas flow. Taking as a typical situation $I_p = 300$ A, M = 30 mg, $R_w = 0.6$ mm, and $v_w = 0.1$ m/s, we find $F_{em} \approx 9 \times 10^{-3}$ N, $F_\gamma \approx 4 \times 10^{-3}$ N, M g = $0.3 \times 10^{-3}$ N, and $\mu\ v_w \approx 0.07 \times 10^{-3}$ N. The latter two forces are small and will be neglected. Note that this argument does not hold for DC GMA welding, where currents are lower and drop masses higher.

The drag force was found (Ref. 25) to

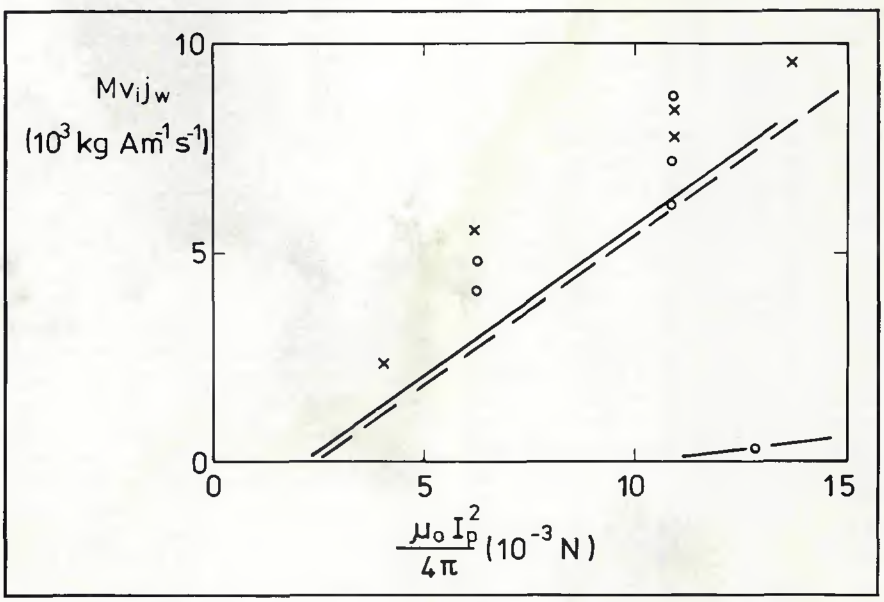


*Fig. 10—Plot to verify Equation 20. Mild steel, $R_c = R_w$. $X - d_w = 1.0$ mm; $o - d_w = 1.2$ mm. — Equation 20 for q = 1.0; $d_w = 1.0$ mm; — — — — same for $d_w = 1.2$ mm; — · — Equation 20 for q = 0.45*

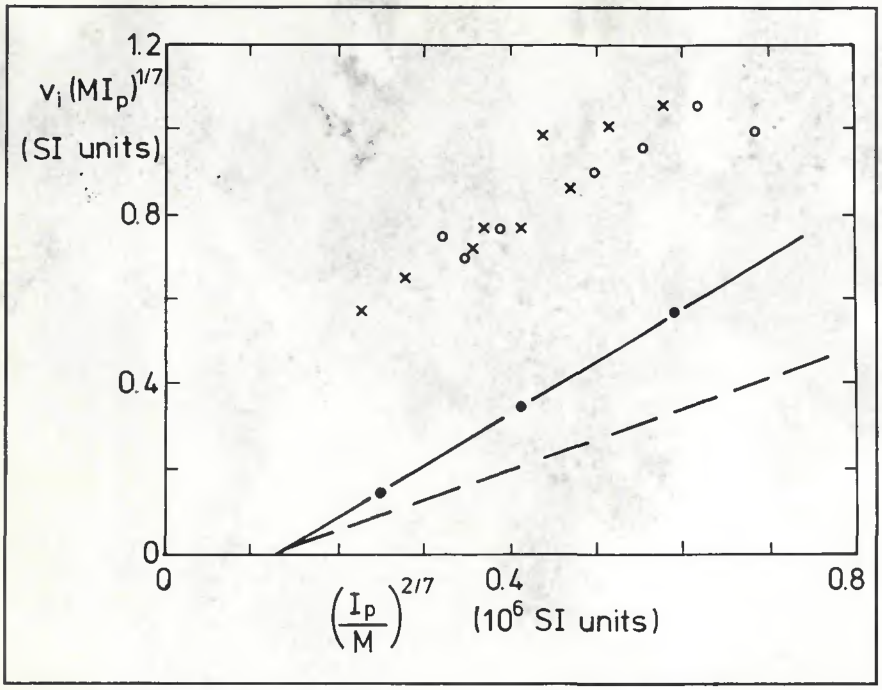


*Fig. 11—As Fig. 9 for Al alloys. $R_c < R_w$, $d_w$ = 1.6 mm. x—AlSi5; o—AlMg5. — — — Equation 19 with q = 1 and $\psi$ = 0.22 (AlSi5). — · — Equation 19 with q = 1 and $\psi$ = 0.15 (AlMg5)*

be of some importance in plasma-GMA experiments, where drop transfer took place in a restricted arc channel. There is no surrounding plasma in the GMA discussed here, and no restricted arc channel, so that the drag force by the gas is negligible. The equation of motion for the detaching drop is

$$M\,\frac{dv}{dt} = F_{em}\,(t) - F_{\gamma}\,(t) \qquad (16)$$

where v is the instantaneous drop velocity. Equation 16 gives

$$M\,(v_i - v_0) = \int_{t_c}^{t_c+\tau} \{F_{em}\,(t) - F_{\gamma}\,(t)\}\,dt \qquad (17)$$

where $v_0 = v(t_c)$, and $\tau = R_c^2/(\alpha R_w^2)$, the time needed to reduce $R_n$ from $R_c$ to zero— Equation 1.

Some of the experimental data give, with Equation 4, values of $R_c$ that exceed $R_w$. This means that the drop immediately becomes unstable at the start of the current pulse. In that case, Equation 4 must be replaced by $R_c = R_w$ with $t_c = 0$.

Substitution of Equations 1, 4, 7, 14 and 15 into Equation 17, and some lengthy but straightforward algebra, gives

$$M\,(v_i - v_0) = \frac{\pi\,\beta^2}{\psi}\sqrt{\frac{\rho}{\mu_0}} \left\{\frac{\mu_0\,q^2}{4\pi}\,M^{4/7}\,I_p^{11/7} - \frac{4\pi\,\gamma\,\beta\,M^{6/7}}{3\,I_p^{1/7}}\right\} \qquad (18)$$

which holds for $t_c > 0$. In order to make it possible to compare Equation 18 with the experimental data, we rewrite it as

$$(v_i - v_0)\,(M\,I_p)^{1/7} = \frac{\pi\,\beta^2}{\psi}\sqrt{\frac{\rho}{\mu_0}} \left\{\frac{\mu_0\,q^2}{4\pi}\left(\frac{I_p^6}{M}\right)^{2/7} - \frac{4\pi\,\gamma\,\beta}{3}\right\} \qquad (19)$$

Equation 19 predicts a linear variation of $(v_i - v_0)\,(M\,I_p)^{1/7}$ with $(I_p^6/M)^{2/7}$. The experiments give no information about $v_0$. Therefore, the quantity $v_i\,(M\,I_p)^{1/7}$ is plotted instead in Fig. 9, where $v_i$, M and $I_p$ are as measured for mild steel. This figure also gives points measured by Ludwig, Caron and Pintard (Refs. 3, 4 and 6, respectively), which agree well with the other points, with one exception.

The curve for $v_0 = 0$ was also calculated from Equation 19 with $\beta$ as derived from the other experiment (Table 7) and with either q = 1 or q = 0.45 (see discussion, previous section). Figure 9 also gives these curves. The curve for q = 1 agrees well with the experimental data. This result suggests that the acceleration of the detaching drop in the time before $t = t_c$ is negligible ($v_0 = 0$) and, furthermore, that all the current passes through the drop practically till rupture. Equation 19 is not applicable at low values of the horizontal coordinate in Fig. 9 (low current, high drop mass) because the gravity force was neglected. There, the experimental points must lie above the calculated curve, as is found.

For $R_c = R_w$ ($t_c = 0$), it follows from Equations 1, 7, 14, 15 and 17 that

$$M\,(v_i - v_0)\,j_p = \frac{1}{\psi}\sqrt{\frac{\rho}{\mu_0}}\left\{\frac{q^2\,\mu_0\,I_p^2}{4\pi} - \frac{4\pi\,\gamma\,R_w}{3}\right\} \qquad (20)$$

Figure 10 gives the plot of $M\,v_i\,j_p$ as a function of $\mu_0 I_p^2/(4\pi)$, as derived from the experimental results for mild steel, and the corresponding curve according to Equation 20. The curve predicted for q = 1 lies about 25% below the experimental points, but its slope is in good agreement.

In view of the approximations made in the model, it can be said that this model agrees well with the experimental data for mild steel.

The agreement is less impressive for the aluminum alloys. The experimental curves for the two materials (Fig. 11) coincide and are approximately parallel to the average of the curves predicted by Equation 19. However, the latter curves lie far too low. The most likely cause of the discrepancy is the assumption that $v_0 = 0$. To obtain agreement one has to assume that $v_0$ is about 1 m/s, and this requires an appreciable force, $F_{em}$, when $t < t_c$—Equation 13. This is so if $R_a \approx R_w$. The results for mild steel indicate that $F_{em} \approx 0$ for $t < t_c$, and Equation 13 then gives $R_a/R_w \approx 0.6$. This argument thus leads to the assumption that the anode radius is larger for the aluminum alloys than it is for mild steel. The films (Figs. 4 and 5) show that for $t < t_c$, the drops are cylindrical for the aluminum alloys and conical for the mild steel, which fits in with this assumption.

### Acceleration of Drops in the Arc

This section deals with the results of the DC experiments—Table 6. After detachment, the drops enter the arc and are accelerated in the plasma. Figure 3 shows that the acceleration is practically constant, initially, and that it decreases as the drop approaches the weld pool. This acceleration is caused by the gas flow towards the weld pool. Small drops introduced into the arc will be accelerated by the drag force, and the model of a sphere in a uniform flow field (Ref. 27) is appropriate for them. This model was used by Caron (Ref. 4) and Needham, *et al.* (Ref. 5). However, the radius of the falling drop, $R_f$, always exceeded $R_w$ in the experiments presented here. The drop velocity (typically 1 m/s) is much smaller than the gas flow velocity in this type of arc in the absence of drops (typically 100–1000 m/s, Refs. 23 and 24). Consequently, the gas flow in the arc will be strongly inhibited by the large drops. The

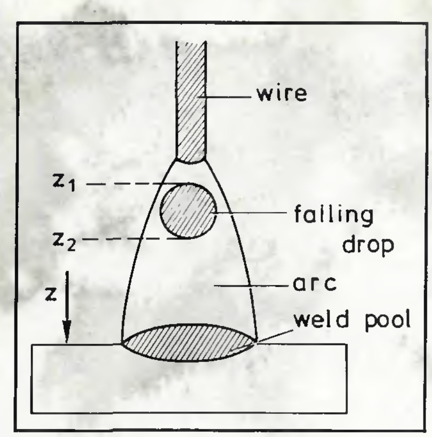


*Fig. 12 — Illustration of discussion of acceleration of drops in arc*

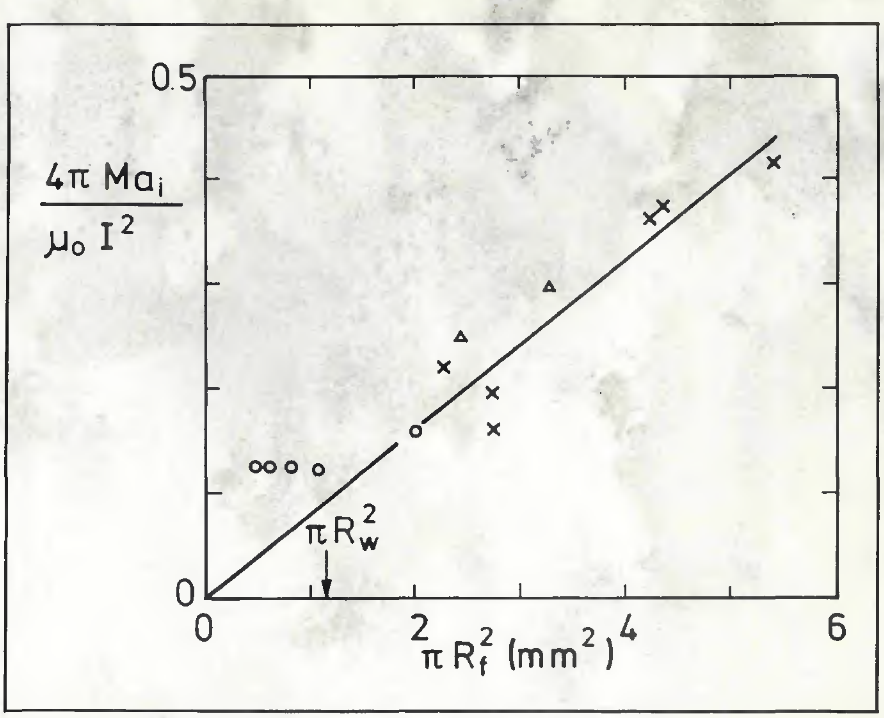


*Fig. 13 — Plot to verify model of drop acceleration, Equation 22. Mild steel, $d_w = 1.2$ mm. x — experimental data from Table 7; Δ — data for $I \geq 200$ A from Ref. 6; o — same from Ref. 4. The slope of the broken line gives, with Equation 22, that $R_{arc} = 2.0$ mm*

following model is proposed for this situation.

Just above the drop ($z = z_1$ in Fig. 12), the flow velocity is low and the static pressure is equal to $p_0 + p_L$ with

$$p_L \approx \frac{\mu_0 I^2}{4\P^2 R^2_{arc}} \qquad (21)$$

where $R_{arc}$ is the arc radius, which varies with z. Below the drop ($z > z_2$ in Fig. 12), there is a fast gas flow towards the weld pool and the stationary gas pressure is close to $p_0$, as was said above. We thus find as an upper limit to the force $F_{pl}$ exerted by the plasma on the drop

$$F_{pl} = \P R_f^2 \frac{\mu_0 I^2}{4\P^2 R^2_{arc}} \qquad (22)$$

Equation 22 is expected to hold when $R_f > R_w$. Figure 13 shows a plot derived from the experimental data (Table 6) drawn in order to verify Equation 22. This equation predicts a straight line for $R_f > R_w$, because $F_{pl} = M a_i$. This linear relation is indeed observed, with $R_{arc} = 2.0$ mm (0.08 in.), which is a reasonable value. Consequently, the experimental data agree with the model proposed.

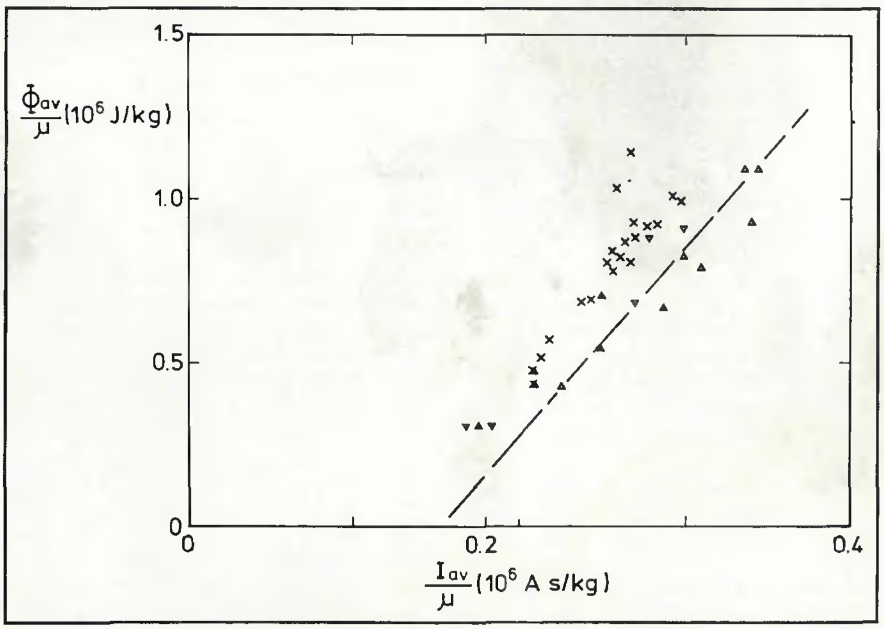


*Fig. 14 — Plot of experimental data used in discussion of heat balance of pendent drop. Mild steel. x — pulsed GMA, $d_w = 1.2$ mm, data from Table 8. Other points DC GMA (Ref. 26); Δ — $d_w = 1.2$ mm; ∇ — $d_w = 1.6$ mm. Broken line gives average for DC operation (Ref. 26)*

**Drop Temperature**

The experimental data on the melting rate allow a comparison between the average drop temperature, $\bar{T}$, in pulsed and in DC operation.

The power required for melting the metal is provided partly by Joule heating in the solid wire and partly by electron absorption at the anode on the liquid tip, followed by convective heat transfer in the pendent drop.

The time average of the power transferred to the solid metal by the latter process, $\Phi_{av}$, is given by (Ref. 26)

$$\Phi_{av} = I_{av} U_w - \mu c_p (\bar{T} - T_m) - \Phi_{ev} \qquad (23)$$

where $U_w$ is an effective work function, $c_p$ the specific heat of the liquid metal, $T_m$ the melting point, and $\Phi_{ev}$ the power loss by evaporation. The effective work function is the sum of the work function and a term that represents the kinetic energy of the absorbed electrons. The first term on the right-hand side in Equation 23 represents the power generated at the wire tip and the second the power absorbed by the liquid metal. The power $\Phi_{av}$ for pulsed operation was derived from the data in Table 8, with the procedure given in Ref. 26. The effective current is to be used in the terms referring to Joule heating in this procedure, and $I_{av}$ in the terms referring to electron absorption.

Equation 23 can be written as

$$\frac{\Phi_{av}}{\mu} = \frac{I_{av}}{\mu} U_w - c_p (\bar{T} - T_m) - \frac{\Phi_{ev}}{\mu} \qquad (24)$$

Figure 14 gives $\Phi_{av}/\mu$ as a function of $I_{av}/\mu$ for pulsed and DC operation with mild steel wire. The data for the pulsed process show less scatter, which indicates a more stable process. Furthermore, it is seen that the points for the pulsed process lie higher.

For a fixed value of $I_{av}/\mu$, Equation 24 gives

$$\left(\frac{\Phi_{av}}{\mu}\right)_p - \left(\frac{\Phi_{av}}{\mu}\right)_{dc} = c_p\left(\overline{T}_{dc} - \overline{T}_p\right) + \left(\frac{\Phi_{ev}}{\mu}\right)_{dc} - \left(\frac{\Phi_{ev}}{\mu}\right)_p \qquad (25)$$

where the subscripts p and dc indicate pulsed and DC operation, respectively. As a higher drop temperature corresponds to a higher evaporation rate, and Fig. 14 shows that the left-hand side of Equation 25 is positive, it follows that $\overline{T}$ is higher by 100° to 200° C (180° to 360°F) during DC operation than during pulsed operation. This result was also obtained by calorimetric measurements (Refs. 28, 29).

## Conclusions

In pulsed-arc welding, the pendent drop generally contracts at the start of the current pulse and becomes unstable when a critical radius is reached and a neck is formed. The square of the neck radius decreases linearly with time, the decay time being inversely proportional to the electric current.

The Lorentz force acting after the pendent drop has become unstable accounts for the drop velocity at detachment, if the wire material is mild steel. If the wire material is an aluminum alloy, then another mechanism is operative, which was not identified with certainty.

The acceleration of large drops after detachment can be ascribed to the static arc pressure generated by electromagnetic effects.

Analysis of the heat balance of the pendent drop indicates that the drop temperature is lower in pulsed than in DC GMA welding, which is in agreement with previous work.

## Appendix

### Symbols Used

$a_i$ — acceleration by plasma at detachment, m $s^{-2}$
B — magnetic induction, Wb $m^{-2}$
$c_p$ — specific heat capacity, 1 J $kg^{-1}$ $(°C)^{-1} = 0.239 \times 10^{-3}$ BTU $lb^{-1}$ $(°F)^{-1}$
$d_w$ — wire diameter, 1 m — 39.37 in.
$\vec{f}_L$ — electromagnetic force per unit volume, N $m^{-3}$
$F_1$, $F_2$ — electromagnetic force, N
$F_{em}$ — electromagnetic force on pendent drop
$F_{pl}$ — force by plasma
$F_\gamma$ — surface tension force
I — electric current, A
$I_{eff}$ — effective electric current
$I_n$ — electric current through neck
$I_p$ — electric current during pulse
$I_{av}$ — average electric current
j — current density, A $m^{-2}$
$j_p$ — current density during pulse
K — magnetohydrodynamic parameter
L — length scale, m
$L_d$ — drop length
$L_s$ — extension length, m
M — drop mass, 1 kg = 2.203 lb
$p_0$ — ambient pressure, 1 N $m^{-2} \leftrightarrow 1.4 \times 10^{-4}$ lb $in.^{-2}$
$p_L$ — pressure due to Lorentz force
q — fraction of current passing through neck
r — radial coordinate, m
R — radius, m
$R_a$ — anode radius
$R_{arc}$ — effective arc radius
$R_c$, $R_{cr}$ — critical drop radius
$R_d$ — radius of pendent drop
$R_f$ — radius of drop after detachment
$R_n$ — time-dependent neck radius
$R_w$ — wire radius
t — time, s
$t_c$ — moment of instability
$\overline{T}$ — average drop temperature, °C; T(°F) = 1.8T(°C) + 32
$T_m$ — melting point, °C
u — fluid velocity, 1 m $s^{-1}$ $= 2.36 \times 10^3$ in. $min^{-1}$
v — time-dependent drop velocity, m $s^{-1}$
$v_0$ — drop velocity at moment of instability
$v_f$ — velocity of drop after detachment
$v_i$ — drop velocity with respect to wire, at detachment
$v_w$ — wire velocity
$U_w$ — effective work function, V
z — axial coordinate, m
$\alpha$ — experimental parameter, $s^{-1}$
$\beta$ — parameter for critical drop radius, m $kg^{-2/7}$ $A^{-2/7}$
$\gamma$ — surface tension, N $m^{-1}$
$\mu$ — melting rate, 1 kg $s^{-1}$ = 132.2 lb $min^{-1}$
$\mu_0$ — permeability of vacuum, H $m^{-1}$
$\upsilon$ — kinematic viscosity, $m^2$ $s^{-1}$
$\rho$ — mass density, 1 kg $m^{-3} = 3.61 \times 10^{-5}$ lb $in.^{-3}$
$\sigma$ — electric conductivity, $\Omega^{-1}$ $m^{-1}$
$\tau$ — detachment time, s
$\Phi_{av}$ — average heat flow rate, 1 W $= 56.9 \times 10^{-3}$ BTU $min^{-1}$
$\Phi_{ev}$ — power loss by evaporation, W
$\psi$ — experimental parameter

*References*


1. Oreper, G. M., Eagar, T. W., and Szekely, J. 1983. Convection in arc weld pools. *Welding Journal* 65(11): 307-s to 312-s.

2a. Essers, W. G., and Walter, R. 1981. Heat transfer and penetration mechanism with GMA and plasma-GMA welding. *Welding Journal* 60(2): 37-s to 42-s.

2b. Clark, D., and Howden, D. G. 1984. Fluid flow and penetration in spray-type GMA weld pools. Paper presented at AWS Convention, Dallas, Texas.

3. Ludwig, H. C. 1957. Metal transfer characteristics in gas-shielded arc welding. *Welding Journal* 36(1): 23-s to 26-s.

4. Caron, V. Study of drop motion in the mild steel-argon arc welding system. *Canadian Metallurgical Quarterly* 9(1): 373-380.

5. Needham, J. C., Cooksey, C. J., and Milner, D. R. 1960. Metal transfer in inert-gas shielded arc welding. *Brit. Weld. J.* 7: 101-114.

6. Pintard, J. 1967. Caractéristiques de la fusion et du transfert dans le procédé MIG de soudage de l'acier sous argon. *Soudage et Techniques Connexes* 21: 381-393.

7. Jilong Ma and Apps, R. L. 1983. Analyzing metal transfer during MIG welding. *Welding and Metal Fabrication* 51: 119-128.

8. Lancaster, J. F. 1980. *Metallurgy of Welding*. London, England, Allen and Unwin.

9. Murty, G. S. 1960. Instability of conducting fluid cylinder due to axial current. *Arkiv för Fysik* 18 (14) 241-250.

10. Maecker, H. 1955. Plasmaströmungen in lichtbögen infolge eigenmagnetischer kompression. *Z. Physik* 141: 198-216.

11. Greene, W. J. 1960. An analysis of transfer in gas-shielded welding arcs. *AIEE Trans., Part II: Applications and Industry* 79: 194-203.

12. Amson, J. C. 1965. Lorentz force in the molten tip of an arc electrode. *Brit. J. Appl. Phys.* 16: 1169-1179.

13. Needham, J. C. 1963. Simple 1000 f.p.s. framing camera without optical compensation. *Proc. 6th Int. Conf. on High-Speed Photography*, The Hague, eds. J. G. A. de Graaf and P. Tegelaar, pp. 41-44, Haarlem, Holland, Tjeenk Willink.

14. Lanczos, C. 1956. *Applied Analysis*. Englewood Cliffs N. J., Prentice Hall.

15. Woods, R. A. 1980. Metal transfer in aluminum alloys. *Welding Journal* 59(2): 59-s to 66-s.

16. Dattner, A., Lehnert, B., and Lundquist, S. 1958. Liquid conductor model of instabilities in a pinched discharge. *Proc. 2nd UN Conference on the Peaceful Uses of Atomic Energy*, Geneva, Switzerland, Vol. 31, pp. 325-327. Pergamon Press.

17. Lancaster, J. F., ed. 1984. *The Physics of Welding*. Oxford, England, Pergamon Press.

18. Kohlhaas, R. 1965. Die magnetische suszeptibilität von eisen, kobalt und nickel bei hohen temperaturen und das magnetische verhalten des austenits. *Archiv für das Eisenhüttenwesen* 36(6): 437-448.

19. Shercliff, J. A. 1970. Fluid motions due to an electric current source. *J. Fluid Mech.* 40(2): 241-250.

20. Ando, K., and Nishiguchi, K. 1968. Mechanism of formation of pencil-point-like wire tip in MIG arc welding. IWW Doc. 212-156-68.

21. Waszink, J. H., and Van den Heuvel, G. J. P. M. 1979. Measurements and calculations of the resistance of the wire extension in arc welding. *Proc. Int. Conf. on Arc Physics and Weld Pool Behaviour*, pp. 227-239, London, England, The Welding Institute, Abington, Cambridge.

22. Lev, M. L., and Peregud, B. P. 1977. Growth time of the MHD sausage instability in a liquid conductor. *Sov. Phys. Tech. Phys.* 22(10): 1229-1232.

23. Wienecke, R. 1955. Über das geschwindigkeitsfeld der hochstromkohlebogensaüle. *Z. Physik* 143: 128-140.

24. McKelliget, J., Szekely, J., Vardelle, M., and Fauchais, P. 1982. Temperature and velocity fields in a gas stream exciting a plasma torch. A mathematical model and its experimental verification. *Plasma Chemistry and Plasma Processing* 2(3): 317-332.

25. Waszink, J. H., and Graat, L. H. J. 1983. Experimental investigation of the forces acting on a drop of weld metal. *Welding Journal* 62(4): 108-s to 116-s.

26. Waszink, J. H., and Van den Heuvel, G. J. P. M. 1982. Heat generation and heat flow in the filler metal in GMA welding. *Welding Journal* 61(8): 269-s to 282-s.

27. Schlichting, H. 1968. *Boundary-Layer Theory*, 6th ed. New York, N. Y., McGraw-Hill.

28. Heiro, H., and North, T. H. 1976. The influence of welding parameters on droplet temperature during pulsed arc welding. *Welding and Metal Fabrication* (9): 482-485, 518.

29. Maruo, H., and Hirata, Y. 1984. Study on pulsed MIG welding. IIW Doc. SG212-585-84.

30. Smithells, C. J., and Brandes, E. A. 1976. *Metals Reference Book*, 5th Ed. London, England, Butterworths.